

# Origin of competing charge density waves in kagome metal $\text{ScV}_6\text{Sn}_6$

Kang Wang,<sup>1</sup> Siyu Chen,<sup>1,2</sup> Sun-Woo Kim,<sup>1,\*</sup> and Bartomeu Monserrat<sup>1,2,†</sup>

<sup>1</sup>*Department of Materials Science and Metallurgy, University of Cambridge,  
27 Charles Babbage Road, Cambridge CB3 0FS, United Kingdom*

<sup>2</sup>*Cavendish Laboratory, University of Cambridge,  
J. J. Thomson Avenue, Cambridge CB3 0HE, United Kingdom*

Understanding competing charge density wave (CDW) orders in the bilayer kagome metal  $\text{ScV}_6\text{Sn}_6$  remains a challenge. Experimentally, upon cooling, short-range CDW order with the wave vector  $\mathbf{q}_2 = (\frac{1}{3}, \frac{1}{3}, \frac{1}{2})$  is observed, which is subsequently suppressed by the condensation of the long-range CDW order  $\mathbf{q}_3 = (\frac{1}{3}, \frac{1}{3}, \frac{1}{3})$  at lower temperature. In conflict with these observations, theoretical calculations overestimate the transition temperature by a few thousand Kelvin and incorrectly predict the  $\mathbf{q}_2$  CDW order to be the ground state. Here, we develop a theory of CDW order in  $\text{ScV}_6\text{Sn}_6$  based on anharmonic phonon-phonon calculations combined with density functional theory. We predict a temperature-driven phase transition from the high-temperature  $\mathbf{q}_2$  CDW to the low-temperature  $\mathbf{q}_3$  CDW order, fully explaining experimental observations. Additionally, we clarify that both multi-phonon effects and semi-core electron states play a crucial role in stabilizing the  $\mathbf{q}_3$  order. Finally, we construct a phase diagram of the competing CDWs in the lattice parameter space and demonstrate that the out-of-plane lattice parameter plays a pivotal role in manipulating the competing CDWs in  $\text{ScV}_6\text{Sn}_6$ , motivating us to propose compressive bi-axial strain as an experimental protocol to stabilize the  $\mathbf{q}_2$  CDW order. Our work provides a full theory of CDWs in  $\text{ScV}_6\text{Sn}_6$ , rationalizing experimental observations and resolving earlier discrepancies between theory and experiment. Overall, our work contributes to the wider effort of understanding CDWs in the kagome metal family.

Kagome materials have emerged as promising platforms to study novel quantum phases of matter that arise from the interplay between lattice geometry, band topology, and electronic correlations [1–3]. Typical electronic band structures of kagome materials include Dirac points, flat bands, and van Hove singularities, serving as rich sources for a variety of structural and electronic instabilities [4–8]. Indeed, exotic electronic states such as superconductivity [9–11], charge density waves (CDWs) [9, 12–15], pair density waves [16], non-trivial topological states [9, 17], and electronic nematicity [18], have been observed in representative kagome metals  $\text{AV}_3\text{Sb}_5$  ( $A=\text{K}, \text{Rb}, \text{and Cs}$ ) [19]. Of these, the CDW state exhibits unconventional properties including time-reversal and rotational symmetry breaking [12, 18, 20–26], and an unconventional interplay with superconductivity featuring a double superconducting dome [27–30]. This has sparked remarkable interest and controversy, prompting the exploration of other material candidates in the quest for a comprehensive understanding of the CDW state in kagome materials.

In this context, the newly discovered bilayer kagome metals  $\text{RV}_6\text{Sn}_6$  ( $R$  is a rare-earth element) have attracted much attention [31–51]. Among the  $\text{RV}_6\text{Sn}_6$  series, the non-magnetic  $\text{ScV}_6\text{Sn}_6$  compound is the only one that has been reported to undergo a CDW transition, which occurs below  $T_{\text{CDW}} \approx 92 \text{ K}$  [38]. The wave vector  $\mathbf{q}_3 = (\frac{1}{3}, \frac{1}{3}, \frac{1}{3})$ , often described as corresponding to a  $\sqrt{3} \times \sqrt{3} \times 3$  periodicity in real space, has been identified as the ordering vector of the CDW state through x-ray diffraction (XRD) [38], neutron diffraction [38], and inelastic x-ray scattering (IXS) [39, 40]. The in-plane

$\sqrt{3} \times \sqrt{3}$  periodicity has been further confirmed using surface-sensitive techniques such as scanning tunnelling microscopy [41, 42] and angle-resolved photoemission spectroscopy [42, 43]. It has also been established that the CDW distortion is dominated by out-of-plane displacements of Sc and Sn atoms [38, 47], which exhibit strong electron-phonon coupling [40, 42, 48]. Interestingly, short-range CDW order with  $\mathbf{q}_2 = (\frac{1}{3}, \frac{1}{3}, \frac{1}{2})$ , corresponding to  $\sqrt{3} \times \sqrt{3} \times 2$  periodicity, has been detected above  $T_{\text{CDW}}$ , but it is suppressed below  $T_{\text{CDW}}$  when the dominant  $\mathbf{q}_3$  CDW develops [40, 48].

On the theoretical front, density functional theory (DFT) calculations have reproduced the competing CDW orders [47], but all previous DFT studies have found that the  $\mathbf{q}_2$  CDW order is the lowest energy ground state [39, 47, 52–54], in stark contrast to experimental reports. Moreover, calculations using the electronic temperature to predict the CDW transition significantly overestimate the temperature scale of the transition, deviating from experimental values by thousands of degrees [54]. These discrepancies between theoretical models and experimental observations pose a key challenge to achieving a comprehensive understanding of CDW states in bilayer kagome metals.

In this work, we present a theory of CDW order in  $\text{ScV}_6\text{Sn}_6$  that explains the reported experimental observations and resolves earlier discrepancies between theory and experiment. Our theory is based on the inclusion of anharmonic phonon-phonon interactions, and captures the observed temperature dependence of charge orders, with a  $\mathbf{q}_2$  distortion occurring at a higher temperature that is subsequently suppressed by the dominant low-

temperature  $\mathbf{q}_3$  charge ordering. In addition, we calculate a phase diagram comparing the two charge orders as a function of the in-plane and out-of-plane lattice parameters, and suggest a clear pathway for using compressive bi-axial strain to experimentally stabilize a CDW with a dominant  $\mathbf{q}_2$  wave vector in  $\text{ScV}_6\text{Sn}_6$ . Finally, we explain the failure of earlier theoretical models by highlighting that the relative stability of the competing CDW states in  $\text{ScV}_6\text{Sn}_6$  exhibits a complex dependence on multi-phonon effects, on the number of valence electrons included in the calculations, and on the out-of-plane lattice parameter.

The high temperature pristine phase of  $\text{ScV}_6\text{Sn}_6$  crystallizes in the hexagonal space group  $P6/mmm$  [Fig. 1(a)]. The primitive cell contains one Sc atom (Wyckoff position  $1a$ ), six equivalent V atoms ( $6i$ ), and three pairs of nonequivalent Sn atoms, labelled as Sn1 ( $2e$ ), Sn2 ( $2d$ ), and Sn3 ( $2c$ ). The crystal structure consists of two kagome layers of V and Sn1 atoms, a triangular layer of Sc and Sn3 atoms, and a honeycomb layer of Sn2 atoms. In the two kagome layers, the Sn1 atoms buckle in opposite directions relative to each V kagome sublattice. The Sn1 and Sc atoms form a chain along the  $c$  axis. Notably, the smallest  $R$ -site ion radius of  $\text{ScV}_6\text{Sn}_6$  among the  $RV_6\text{Sn}_6$  series leads to the formation of Sn1-Sc-Sn1 trimers mediated by a shortening of the Sc-Sn1 bonds and an elongation of the Sn1-Sn1 bonds along the chain. This unique structural feature results in more space for the Sn1-Sc-Sn1 trimers to vibrate along the  $c$  direction, a characteristic absent in other  $RV_6\text{Sn}_6$  compounds without a trimer formation, which has been demonstrated to be crucial to the formation of the CDW [44, 48]. Motivated by this observation, the calculations reported below are performed using the PBEsol exchange-correlation functional [55], which gives better agreement with the experimentally measured out-of-plane lattice parameter compared to the often-used PBE exchange-correlation functional [56]. Nonetheless, the overall conclusions of our work are independent of the exchange-correlation functional used, as detailed in the Supplemental Material [57].

Figure 1(d) shows the calculated harmonic and anharmonic phonon dispersions of pristine  $\text{ScV}_6\text{Sn}_6$ . The harmonic phonon dispersion shows multiple dynamical instabilities, which appear as imaginary frequencies in the phonon dispersion [represented by the grey area in Fig. 1(d)]. The harmonic instabilities span a wide region of the Brillouin zone, including the whole  $q_z = \frac{\pi}{c}$  plane represented by the A-L-H-A closed path, and also including other values of  $q_z$ , for example the  $K'$  point at  $q_z = \frac{1}{3}$ . Specifically, the calculated harmonic instabilities include the CDW instabilities reported experimentally with wave vectors  $\mathbf{q}_3$  and  $\mathbf{q}_2$ , which correspond to the  $K'$  and H points of the Brillouin zone, respectively; but also include many other instabilities. Interestingly, when anharmonic phonon-phonon interactions [58–60] are included, most harmonic instabilities disappear and only

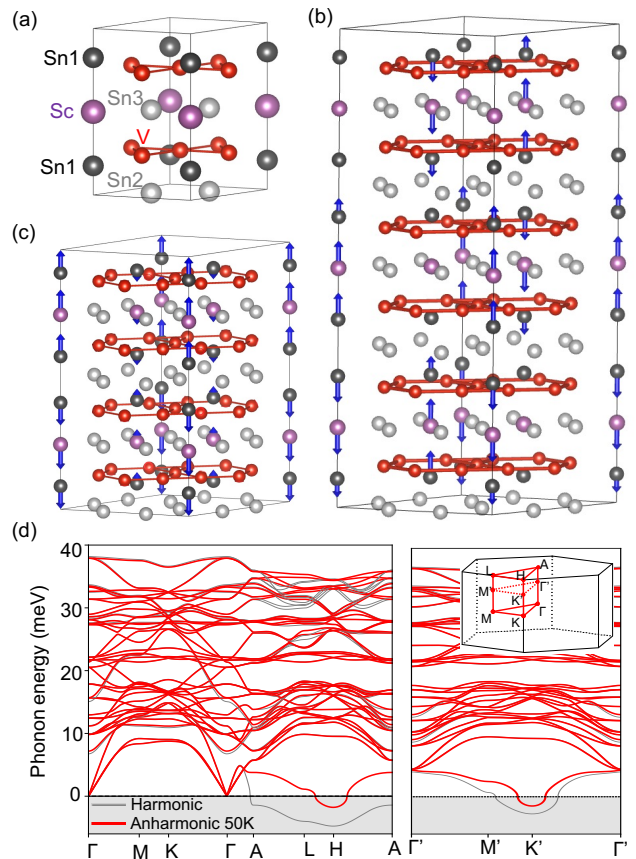


Figure 1. (a) Crystal structure of pristine  $\text{ScV}_6\text{Sn}_6$ . (b),(c) CDW displacement patterns (blue arrows) for the (b)  $\mathbf{q}_3$  ( $\sqrt{3} \times \sqrt{3} \times 3$ ) and (c)  $\mathbf{q}_2$  ( $\sqrt{3} \times \sqrt{3} \times 2$ ) orders. The arrows are calculated through the structural difference of the relaxed CDW structure and the pristine structure. (d) Harmonic (grey) and anharmonic (red) phonon dispersions of pristine  $\text{ScV}_6\text{Sn}_6$ . The inset shows the Brillouin zone of pristine  $\text{ScV}_6\text{Sn}_6$  with certain high symmetry points labelled. The prime notation designates the high symmetry points on the  $q_z = \frac{1}{3}$  plane.

two remain: those at the  $K'$  and H points of the Brillouin zone. These are the instabilities reported experimentally, which are fully recovered by our calculations.

Figures 1(b) and 1(c) illustrate the CDW structures optimized along the imaginary phonon modes at  $\mathbf{q}_3$  and  $\mathbf{q}_2$ , respectively. The distortions of both CDW orders mainly occur along the Sn1-Sc chains, where the Sn1-Sc-Sn1 trimers are displaced to form  $\times 3$  and  $\times 2$  CDW periodicities along the  $c$  axis for the  $\mathbf{q}_3$  and  $\mathbf{q}_2$  orders, respectively. The  $\mathbf{q}_3$  CDW order involves three trimers exhibiting a stationary-up-down pattern while the  $\mathbf{q}_2$  CDW order involves two trimers with an up-down pattern. In both CDW orders, the trimers in one Sc1-Sn chain alternate their displacement along the  $c$  axis relative to the other Sc1-Sn chains, resulting in the  $\sqrt{3} \times \sqrt{3}$  in-plane periodicity.

To further characterize the CDW of  $\text{ScV}_6\text{Sn}_6$ , we investigate the temperature dependence of phonon dispersions using anharmonic calculations within the stochastic self-consistent harmonic approximation [58–60]. Figure 2(a) displays the anharmonic phonon dispersion of pristine  $\text{ScV}_6\text{Sn}_6$  at temperatures of 0 K, 50 K, 100 K and 200 K. The majority of phonon branches show a negligible temperature dependence, with the key exception of a pronounced softening of the lowest energy phonon branch at  $\mathbf{q}_2$  (H point) and  $\mathbf{q}_3$  ( $\text{K}'$  point) upon cooling. The squared frequency  $\omega^2$  of the soft modes should exhibit a linear behaviour with respect to temperature near the vanishing point [61], and we use a linear fit to extract the transition temperatures  $T^*$  associated with each phonon softening [Fig. 2(b)]. At high temperature (200 K), the pristine  $\text{ScV}_6\text{Sn}_6$  phase is dynamically stable and the phonon frequencies at both  $\mathbf{q}$  vectors are real. Interestingly, the frequency at  $\mathbf{q}_2$  becomes imaginary at a higher temperature of 140 K compared to the temperature of 84 K at which the frequency at  $\mathbf{q}_3$  becomes imaginary. This implies that, starting from the high temperature pristine phase, the first distortion to develop with decreasing temperature is that associated with  $\mathbf{q}_2$ , rationalizing the short-range  $\mathbf{q}_2$  order above the  $\mathbf{q}_3$  CDW transition temperature observed in XRD [48] and IXS [40].

Our work proposes a novel mechanism underlying the observed series of temperature-induced CDW transitions. Our anharmonic phonon results exhibit remarkable quantitative agreement with experimental data [Fig. 2(b)], in stark contrast to the significant overestimation of temperature scales (with critical temperatures of 2,000 K and 5,500 K) obtained by adjusting electronic temperature via changing smearing values in harmonic phonon calculations as used in a previous work [54] (see also SM [57]). This clearly demonstrates that the transition is driven by ionic entropy resulting from anharmonic phonon-phonon interactions, rather than electronic entropy.

Comparing the calculated Helmholtz free energy between the  $\mathbf{q}_2$  and  $\mathbf{q}_3$  CDW orders, we observe a crossover from  $\mathbf{q}_2$  to  $\mathbf{q}_3$  CDWs [Fig. 2(c)]. The  $\mathbf{q}_2$  CDW order is more stable at high temperature and the free energy difference decreases as the temperature decreases. The crossover occurs approximately at  $T_c = 42$  K, which is lower than the onset of the  $\mathbf{q}_3$  CDW instability  $T^* = 84$  K in Fig. 2(b). The predicted transition temperature  $T_c$  of the  $\mathbf{q}_3$  CDW ( $\approx 42$  K) is lower than experimental values of 92 K [62] and 84 K [48]. This quantitative discrepancy is attributed to the sensitivity of  $T_c$  on the volume of the system, as discussed in detail below, and more generally to the inherent temperature-independent limitations of DFT calculations, such as those arising from the choice of exchange-correlation functional. At 0 K, the  $\mathbf{q}_3$  CDW structure is more stable by 1.26 meV/f.u. compared to the  $\mathbf{q}_2$  CDW structure.

Our DFT calculations correctly predict the  $\mathbf{q}_3$  CDW

to be the lowest energy ground state, consistent with experiments [38–40, 48]. Puzzlingly, all earlier DFT studies [47, 52, 53] had predicted the  $\mathbf{q}_2$  distortion to be the ground state, in stark contrast to the experimental reports and to our results. To rationalize this, we highlight that in our calculations we have established that both multi-phonon effects and the inclusion of electronic semi-core states in the valence are necessary to stabilize the  $\mathbf{q}_3$  CDW order [Fig. 3]. When the pristine structure is distorted along a single imaginary phonon mode at a specific  $\mathbf{q}$  point, the energy of the system decreases and the structure distorted along the  $\mathbf{q}_2$  vector has lower energy than that distorted along the  $\mathbf{q}_3$  vector by 0.29 meV/f.u., which is consistent with previous DFT calculations [47]. When these single-mode distorted structures are fully relaxed, equivalent to adding distortions along additional phonon modes, the total energy of both CDW structures decreases further. Under this multi-phonon relaxation, the  $\mathbf{q}_2$  CDW structure remains lower in energy compared to the  $\mathbf{q}_3$  CDW structure by 0.48 meV/f.u.

Additionally, we test a standard pseudopotential with valence electrons  $3d^14s^2$  for Sc atoms and  $5s^25p^2$  for Sn atoms, and also a pseudopotential that also includes the  $s$  and  $p$  semi-core states in Sc atoms and the  $d$  semi-core states in Sn atoms to the valence states. Only with the latter pseudopotential does the  $\mathbf{q}_3$  CDW structure become more stable compared to the  $\mathbf{q}_2$  CDW structure, by 0.47 meV/f.u. The inclusion of semi-core states changes the bond lengths of the Sn1-Sc chains along the

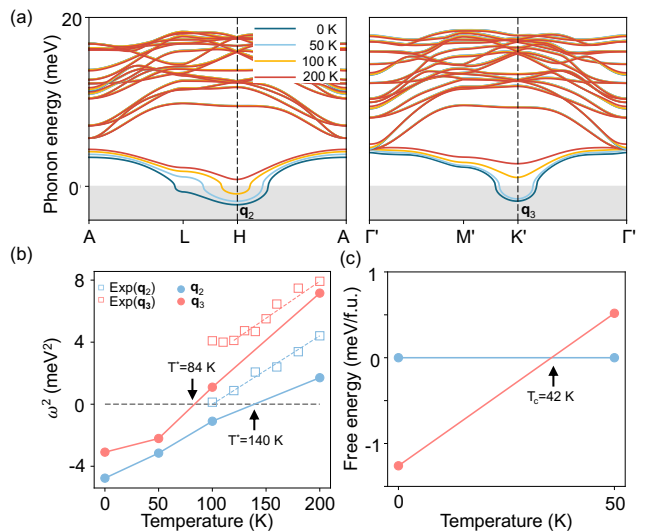


Figure 2. (a) Anharmonic phonon dispersions at 0 K, 50 K, 100 K, and 200 K. (b) Squared phonon frequency  $\omega^2$  of the lowest energy phonon modes at the H and  $\text{K}'$  points with respect to ionic temperature. The calculated anharmonic frequencies are shown in circles and the experimental results [40] are represented by squares. (c) Relative Helmholtz free energy as a function of temperature for the two CDW structures.

c axis, specifically the spacing between adjacent Sn1-Sc-Sn1 trimers decreases by 0.01 Å. This structural change reduces the space available for vibration of Sn1-Sc-Sn1 trimers along the c direction and thus increases the energy of both structures associated with the charge orders. Of the two atomic distortion patterns, that associated with  $\mathbf{q}_2$  requires more space between Sn1-Sc-Sn1 trimers because every trimer is out-of-phase with adjacent trimers. By contrast, the longer wavelength distortion associated with  $\mathbf{q}_3$  requires less space, which explains why the energy increase of the  $\mathbf{q}_2$  structure is larger than that of the  $\mathbf{q}_3$  structure. In the calculations reported above, we used the pseudopotential with semi-core states in the valence.

It is important to highlight that multi-phonon effects play an equally important role compared to semi-core electron states in stabilizing the  $\mathbf{q}_3$  structure compared to the  $\mathbf{q}_2$  structure. As also shown in Fig. 3, when the two competing CDW structures are only distorted along the corresponding single imaginary phonon modes, the inclusion of semi-core electronic states in the valence is not enough to reach the  $\mathbf{q}_3$  ground state. In this case, only after multi-phonon terms are also included do we recover the correct energy ordering with the  $\mathbf{q}_3$  ground state. Overall, this implies that *both* multi-phonon terms and the inclusion of semi-core electron states in the valence are necessary to obtain a theoretical model that correctly predicts the ground state CDW order of ScV<sub>6</sub>Sn<sub>6</sub>. This explains and resolves the outstanding discrepancy between theory and experiment, and provides a foundation for the predictive model of the CDW state in bilayer kagome ScV<sub>6</sub>Sn<sub>6</sub> described above.

Having established the correct theory of the competing CDWs in ScV<sub>6</sub>Sn<sub>6</sub>, we explore the phase diagram in lattice parameter space which provides important insights for manipulating the competing CDWs. Figure 4(a) shows a phase diagram of the  $\mathbf{q}_2$  and the  $\mathbf{q}_3$  CDW orders

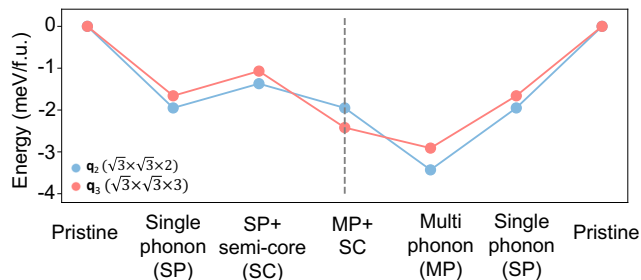


Figure 3. Total energy of the  $\mathbf{q}_2$  and  $\mathbf{q}_3$  CDW structures compared to the pristine structure. Single phonon (SP) and multiple phonon (MP) indicate CDW structures distorted according to the atomic displacement pattern associated with a single phonon mode or with multiple phonon modes, respectively. Semi-core (SC) refer to calculations in which *s* and *d* semi-core states in Sc atoms are treated as valence states.

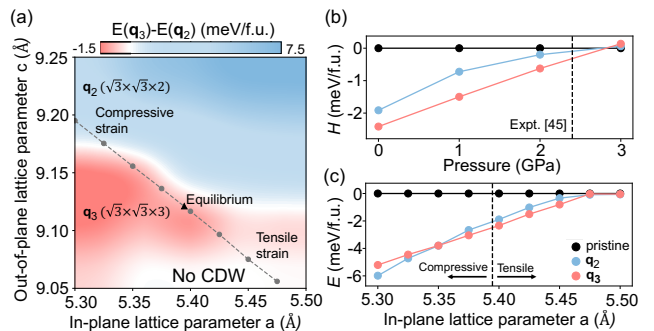


Figure 4. (a) Phase diagram of the competing  $\mathbf{q}_2$  and  $\mathbf{q}_3$  CDW orders in the in-plane and out-of-plane lattice parameter space. Color bar represents the total energy difference between the  $\mathbf{q}_2$  and  $\mathbf{q}_3$  structures. The grey dashed line shows the change of lattice parameters under in-plane biaxial strain. (b) Relative enthalpy  $H = E + PV$  of the  $\mathbf{q}_2$  and  $\mathbf{q}_3$  CDWs to pristine structure. Vertical dashed line indicates the experimental value of critical pressure of 2.4 GPa that CDW orders are totally suppressed [45]. (c) Total energy of the  $\mathbf{q}_2$  and  $\mathbf{q}_3$  CDWs as a function of in-plane biaxial strain.

as a function of the in-plane and out-of-plane lattice parameters. We find that the out-of-plane lattice parameter holds the key to control competing the CDW orders. This can be rationalized by noting that the out-of-plane lattice parameter determines the space available for the distortions of adjacent Sn1-Sc-Sn1 trimers and thus dominates the energetics between competing CDWs. A smaller out-of-plane lattice parameter restricts the available space for Sn1-Sc-Sn1 trimers to distort, favoring an additional stationary configuration of trimers in  $\mathbf{q}_3$  CDW. Conversely, a larger out-of-plane lattice parameter facilitates the collective distortions of trimers and favours the  $\mathbf{q}_2$  CDW. We note that some earlier DFT studies [39, 54] that considered semi-core states failed to accurately predict the  $\mathbf{q}_3$  CDW as the ground state because they used larger out-of-plane lattice parameters compared to experimental values (see SM [57] for details).

Finally, we discuss the effects of the hydrostatic pressure and in-plane biaxial strain on the competing CDWs. Hydrostatic pressure suppresses both CDW orders [Fig. 4(b)], as increasing pressure decreases the out-of-plane lattice parameter and thus the space available for Sn1-Sc-Sn1 trimers to distort. Our theoretical value for the critical pressure ( $\approx 2.8$  GPa) at which the  $\mathbf{q}_3$  CDW disappears is in remarkable agreement with the experimental value of 2.4 GPa [45]. Similarly, in-plane biaxial tensile strain leads to a decrease in the out-of-plane lattice parameter, suppressing both CDW orders [Fig. 4(c)]. By contrast, in-plane compressive strain increases the out-of-plane lattice parameter, enhancing the stability of both CDW orders. Interestingly, the  $\mathbf{q}_2$  CDW order becomes the ground state under the compressive strain. The predicted value of critical compressive strain

is just around 1%, which should be experimentally accessible. These predictions warrant further experimental studies to corroborate our findings.

In conclusion, we have demonstrated the decisive role of temperature, captured by anharmonic phonon-phonon interactions, and volume, on the competition between the  $\mathbf{q}_2$  and  $\mathbf{q}_3$  charge orders in  $\text{ScV}_6\text{Sn}_6$ . Our work fully resolves the controversy between previous theoretical and experimental studies: a correct theoretical description of CDW order requires the inclusion of multi-phonon effects, semi-core electron states as valence, and the use of a correct out-of-plane  $c$  lattice parameter. Our theory also elucidates the experimentally observed temperature-induced CDW phase transition from a high temperature  $\mathbf{q}_2$  to a low temperature  $\mathbf{q}_3$  order. Finally, we predict that in-plane biaxial strain can be used to manipulate the competing CDW orders, and propose that compressive strain could be used to experimentally discover a regime in which the  $\mathbf{q}_2$  CDW dominates. More generally, our findings contribute to the wider effort of understanding kagome metals that host multiple CDW instabilities, such as those in the recently discovered room temperature CDW kagome metal  $\text{LaRu}_3\text{Si}_2$  [63, 64].

K.W., S.-W.K., and B.M. are supported by a UKRI Future Leaders Fellowship [MR/V023926/1], and S.C. and B.M. are supported by a EPSRC grant [EP/V062654/1]. S.C. also acknowledges financial support from the Cambridge Trust and from the Winton Programme for the Physics of Sustainability. B.M. also acknowledges support from the Gianna Angelopoulos Programme for Science, Technology, and Innovation, and from the Winton Programme for the Physics of Sustainability. The computational resources were provided by the Cambridge Tier-2 system operated by the University of Cambridge Research Computing Service and funded by EPSRC [EP/P020259/1] and by the UK National Supercomputing Service ARCHER2, for which access was obtained via the UKCP consortium and funded by EPSRC [EP/X035891/1].

---

\* [swk38@cam.ac.uk](mailto:swk38@cam.ac.uk)

† [bm418@cam.ac.uk](mailto:bm418@cam.ac.uk)

- [1] J.-X. Yin, S. H. Pan, and M. Zahid Hasan, *Nat. Rev. Phys.* **3**, 249 (2021).
- [2] T. Neupert, M. M. Denner, J.-X. Yin, R. Thomale, and M. Z. Hasan, *Nat. Phys.* **18**, 137 (2022).
- [3] K. Jiang, T. Wu, J.-X. Yin, Z. Wang, M. Z. Hasan, S. D. Wilson, X. Chen, and J. Hu, *Nat. Sci. Rev.* **10**, nwac199 (2022).
- [4] J. Wen, A. Rüegg, C.-C. J. Wang, and G. A. Fiete, *Phys. Rev. B* **82**, 075125 (2010).
- [5] E. Tang, J.-W. Mei, and X.-G. Wen, *Phys. Rev. Lett.* **106**, 236802 (2011).
- [6] K. Sun, Z. Gu, H. Katsura, and S. Das Sarma, *Phys. Rev. Lett.* **106**, 236803 (2011).
- [7] M. L. Kiesel, C. Platt, and R. Thomale, *Phys. Rev. Lett.* **110**, 126405 (2013).
- [8] W.-S. Wang, Z.-Z. Li, Y.-Y. Xiang, and Q.-H. Wang, *Phys. Rev. B* **87**, 115135 (2013).
- [9] B. R. Ortiz, S. M. L. Teicher, Y. Hu, J. L. Zuo, P. M. Sarte, E. C. Schueller, A. M. M. Abeykoon, M. J. Krogstad, S. Rosenkranz, R. Osborn, R. Seshadri, L. Balents, J. He, and S. D. Wilson, *Phys. Rev. Lett.* **125**, 247002 (2020).
- [10] B. R. Ortiz, P. M. Sarte, E. M. Kenney, M. J. Graf, S. M. L. Teicher, R. Seshadri, and S. D. Wilson, *Phys. Rev. Mater.* **5**, 034801 (2021).
- [11] Q. Yin, Z. Tu, C. Gong, Y. Fu, S. Yan, and H. Lei, *Chin. Phys. Lett.* **38**, 037403 (2021).
- [12] Y.-X. Jiang, J.-X. Yin, M. M. Denner, N. Shumiya, B. R. Ortiz, G. Xu, Z. Guguchia, J. He, M. S. Hossain, X. Liu, J. Ruff, L. Kautzsch, S. S. Zhang, G. Chang, I. Belopolski, Q. Zhang, T. A. Cochran, D. Multer, M. Litskevich, Z.-J. Cheng, X. P. Yang, Z. Wang, R. Thomale, T. Neupert, S. D. Wilson, and M. Z. Hasan, *Nat. Mater.* **20**, 1353 (2021).
- [13] H. Tan, Y. Liu, Z. Wang, and B. Yan, *Phys. Rev. Lett.* **127**, 046401 (2021).
- [14] H. Zhao, H. Li, B. R. Ortiz, S. M. L. Teicher, T. Park, M. Ye, Z. Wang, L. Balents, S. D. Wilson, and I. Zeljkovic, *Nature* **599**, 216 (2021).
- [15] Z. Liang, X. Hou, F. Zhang, W. Ma, P. Wu, Z. Zhang, F. Yu, J.-J. Ying, K. Jiang, L. Shan, Z. Wang, and X.-H. Chen, *Phys. Rev. X* **11**, 031026 (2021).
- [16] H. Chen, H. Yang, B. Hu, Z. Zhao, J. Yuan, Y. Xing, G. Qian, Z. Huang, G. Li, Y. Ye, S. Ma, S. Ni, H. Zhang, Q. Yin, C. Gong, Z. Tu, H. Lei, H. Tan, S. Zhou, C. Shen, X. Dong, B. Yan, Z. Wang, and H.-J. Gao, *Nature* **599**, 222 (2021).
- [17] Y. Hu, S. M. Teicher, B. R. Ortiz, Y. Luo, S. Peng, L. Huai, J. Ma, N. C. Plumb, S. D. Wilson, J. He, and M. Shi, *Sci. Bull.* **67**, 495 (2022).
- [18] L. Nie, K. Sun, W. Ma, D. Song, L. Zheng, Z. Liang, P. Wu, F. Yu, J. Li, M. Shan, D. Zhao, S. Li, B. Kang, Z. Wu, Y. Zhou, K. Liu, Z. Xiang, J. Ying, Z. Wang, T. Wu, and X. Chen, *Nature* **604**, 59 (2022).
- [19] B. R. Ortiz, L. C. Gomes, J. R. Morey, M. Winiarski, M. Bordelon, J. S. Mangum, I. W. H. Oswald, J. A. Rodriguez-Rivera, J. R. Neilson, S. D. Wilson, E. Ertekin, T. M. McQueen, and E. S. Toberer, *Phys. Rev. Mater.* **3**, 094407 (2019).
- [20] S.-Y. Yang, Y. Wang, B. R. Ortiz, D. Liu, J. Gayles, E. Derunova, R. Gonzalez-Hernandez, L. Šmejkal, Y. Chen, S. S. P. Parkin, S. D. Wilson, E. S. Toberer, T. McQueen, and M. N. Ali, *Sci. Adv.* **6**, eabb6003 (2020).
- [21] M. Kang, S. Fang, J.-K. Kim, B. R. Ortiz, S. H. Ryu, J. Kim, J. Yoo, G. Sangiovanni, D. Di Sante, B.-G. Park, C. Jozwiak, A. Bostwick, E. Rotenberg, E. Kaxiras, S. D. Wilson, J.-H. Park, and R. Comin, *Nat. Phys.* **18**, 301 (2022).
- [22] C. Mielke, D. Das, J.-X. Yin, H. Liu, R. Gupta, Y.-X. Jiang, M. Medarde, X. Wu, H. C. Lei, J. Chang, P. Dai, Q. Si, H. Miao, R. Thomale, T. Neupert, Y. Shi, R. Khasanov, M. Z. Hasan, H. Luetkens, and Z. Guguchia, *Nature* **602**, 245 (2022).
- [23] M. M. Denner, R. Thomale, and T. Neupert, *Phys. Rev. Lett.* **127**, 217601 (2021).
- [24] C. Guo, C. Putzke, S. Konyzheva, X. Huang,

- M. Gutierrez-Amigo, I. Errea, D. Chen, M. G. Vergniory, C. Felser, M. H. Fischer, T. Neupert, and P. J. W. Moll, *Nature* **611**, 461 (2022).
- [25] Y. Xu, Z. Ni, Y. Liu, B. R. Ortiz, Q. Deng, S. D. Wilson, B. Yan, L. Balents, and L. Wu, *Nat. Phys.* **18**, 1470 (2022).
- [26] S.-W. Kim, H. Oh, E.-G. Moon, and Y. Kim, *Nat. Commun.* **14**, 591 (2023).
- [27] K. Y. Chen, N. N. Wang, Q. W. Yin, Y. H. Gu, K. Jiang, Z. J. Tu, C. S. Gong, Y. Uwatoko, J. P. Sun, H. C. Lei, J. P. Hu, and J.-G. Cheng, *Phys. Rev. Lett.* **126**, 247001 (2021).
- [28] F. H. Yu, D. H. Ma, W. Z. Zhuo, S. Q. Liu, X. K. Wen, B. Lei, J. J. Ying, and X. H. Chen, *Nat. Commun.* **12**, 3645 (2021).
- [29] L. Zheng, Z. Wu, Y. Yang, L. Nie, M. Shan, K. Sun, D. Song, F. Yu, J. Li, D. Zhao, S. Li, B. Kang, Y. Zhou, K. Liu, Z. Xiang, J. Ying, Z. Wang, T. Wu, and X. Chen, *Nature* **611**, 682 (2022).
- [30] M. Kang, S. Fang, J. Yoo, B. R. Ortiz, Y. M. Oey, J. Choi, S. H. Ryu, J. Kim, C. Jozwiak, A. Bostwick, E. Rotenberg, E. Kaxiras, J. G. Checkelsky, S. D. Wilson, J.-H. Park, and R. Comin, *Nat. Mater.* **22**, 186 (2023).
- [31] G. Pokharel, S. M. L. Teicher, B. R. Ortiz, P. M. Sarte, G. Wu, S. Peng, J. He, R. Seshadri, and S. D. Wilson, *Phys. Rev. B* **104**, 235139 (2021).
- [32] S. Peng, Y. Han, G. Pokharel, J. Shen, Z. Li, M. Hashimoto, D. Lu, B. R. Ortiz, Y. Luo, H. Li, M. Guo, B. Wang, S. Cui, Z. Sun, Z. Qiao, S. Wilson, and J. He, *Phys. Rev. Lett.* **127**, 266401 (2021).
- [33] H. Ishikawa, T. Yajima, M. Kawamura, H. Mitamura, and K. Kindo, *J. Phys. Soc. Jpn.* **90**, 124704 (2021).
- [34] Y. Hu, X. Wu, Y. Yang, S. Gao, N. C. Plumb, A. P. Schnyder, W. Xie, J. Ma, and M. Shi, *Sci. Adv.* **8**, eadd2024 (2022).
- [35] E. Rosenberg, J. M. DeStefano, Y. Guo, J. S. Oh, M. Hashimoto, D. Lu, R. J. Birgeneau, Y. Lee, L. Ke, M. Yi, and J.-H. Chu, *Phys. Rev. B* **106**, 115139 (2022).
- [36] J. Lee and E. Mun, *Phys. Rev. Mater.* **6**, 083401 (2022).
- [37] D. Di Sante, C. Bigi, P. Eck, S. Enzner, A. Consiglio, G. Pokharel, P. Carrara, P. Orgiani, V. Polewczyk, J. Fujii, P. D. C. King, I. Vobornik, G. Rossi, I. Zeljkovic, S. D. Wilson, R. Thomale, G. Sangiovanni, G. Panaccione, and F. Mazzola, *Nat. Phys.* **19**, 1135 (2023).
- [38] H. W. S. Arachchige, W. R. Meier, M. Marshall, T. Matsuoka, R. Xue, M. A. McGuire, R. P. Hermann, H. Cao, and D. Mandrus, *Phys. Rev. Lett.* **129**, 216402 (2022).
- [39] S. Cao, C. Xu, H. Fukui, T. Manjo, Y. Dong, M. Shi, Y. Liu, C. Cao, and Y. Song, *Nat. Commun.* **14**, 7671 (2023).
- [40] A. Korshunov, H. Hu, D. Subires, Y. Jiang, D. Călugăru, X. Feng, A. Rajapitamahuni, C. Yi, S. Roychowdhury, M. G. Vergniory, J. Stremper, C. Shekhar, E. Vescovo, D. Chernyshov, A. H. Said, A. Bosak, C. Felser, B. A. Bernevig, and S. Blanco-Canosa, *Nat. Commun.* **14**, 6646 (2023).
- [41] S. Cheng, Z. Ren, H. Li, J. S. Oh, H. Tan, G. Pokharel, J. M. DeStefano, E. Rosenberg, Y. Guo, Y. Zhang, Z. Yue, Y. Lee, S. Gorovikov, M. Zonno, M. Hashimoto, D. Lu, L. Ke, F. Mazzola, J. Kono, R. J. Birgeneau, J.-H. Chu, S. D. Wilson, Z. Wang, B. Yan, M. Yi, and I. Zeljkovic, *npj Quantum Mater.* **9**, 1 (2024), publisher: Nature Publishing Group.
- [42] Y. Hu, J. Ma, Y. Li, Y. Jiang, D. J. Gawryluk, T. Hu, J. Teyssier, V. Multian, Z. Yin, S. Xu, S. Shin, I. Plokhikh, X. Han, N. C. Plumb, Y. Liu, J.-X. Yin, Z. Guguchia, Y. Zhao, A. P. Schnyder, X. Wu, E. Pomjakushina, M. Z. Hasan, N. Wang, and M. Shi, *Nat Commun* **15**, 1658 (2024), publisher: Nature Publishing Group.
- [43] S. Lee, C. Won, J. Kim, J. Yoo, S. Park, J. Denlinger, C. Jozwiak, A. Bostwick, E. Rotenberg, R. Comin, M. Kang, and J.-H. Park, *npj Quantum Mater.* **9**, 1 (2024), publisher: Nature Publishing Group.
- [44] W. R. Meier, R. P. Madhugaria, S. Mozaffari, M. Marshall, D. E. Graf, M. A. McGuire, H. W. S. Arachchige, C. L. Allen, J. Driver, H. Cao, and D. Mandrus, *J. Am. Chem. Soc.* **145**, 20943 (2023).
- [45] X. Zhang, J. Hou, W. Xia, Z. Xu, P. Yang, A. Wang, Z. Liu, J. Shen, H. Zhang, X. Dong, Y. Uwatoko, J. Sun, B. Wang, Y. Guo, and J. Cheng, *Materials* **15**, 7372 (2022).
- [46] M. Tuniz, A. Consiglio, D. Puntel, C. Bigi, S. Enzner, G. Pokharel, P. Orgiani, W. Bronsch, F. Parmigiani, V. Polewczyk, P. D. C. King, J. W. Wells, I. Zeljkovic, P. Carrara, G. Rossi, J. Fujii, I. Vobornik, S. D. Wilson, R. Thomale, T. Wehling, G. Sangiovanni, G. Panaccione, F. Cilento, D. Di Sante, and F. Mazzola, *Commun Mater* **4**, 1 (2023), publisher: Nature Publishing Group.
- [47] H. Tan and B. Yan, *Phys. Rev. Lett.* **130**, 266402 (2023).
- [48] G. Pokharel, B. R. Ortiz, L. Kautzsch, S. J. Alvarado Gomez, K. Mallayya, G. Wu, E.-A. Kim, J. P. C. Ruff, S. Sarker, and S. D. Wilson, *Phys. Rev. Mater.* **7**, 104201 (2023).
- [49] S.-H. Kang, H. Li, W. R. Meier, J. W. Villanova, S. Hus, H. Jeon, H. W. S. Arachchige, Q. Lu, Z. Gai, J. Denlinger, R. Moore, M. Yoon, and D. Mandrus, *arXiv* **10.48550/arXiv.2302.14041** (2023).
- [50] K. Shrestha, B. Regmi, G. Pokharel, S.-G. Kim, S. D. Wilson, D. E. Graf, B. A. Magar, C. Phillips, and T. Nguyen, *Phys. Rev. B* **108**, 245119 (2023).
- [51] C. Yi, X. Feng, N. Mao, P. Yanda, S. Roychowdhury, Y. Zhang, C. Felser, and C. Shekhar, *Phys. Rev. B* **109**, 035124 (2024), publisher: American Physical Society.
- [52] S. Liu, C. Wang, S. Yao, Y. Jia, Z. Zhang, and J.-H. Cho, *Phys. Rev. B* **109**, L121103 (2024), publisher: American Physical Society.
- [53] A. Subedi, *Phys. Rev. Mater.* **8**, 014006 (2024), publisher: American Physical Society.
- [54] H. Hu, Y. Jiang, D. Călugăru, X. Feng, D. Subires, M. G. Vergniory, C. Felser, S. Blanco-Canosa, and B. A. Bernevig, *arXiv* **10.48550/arXiv.2305.15469** (2023).
- [55] J. P. Perdew, A. Ruzsinszky, G. I. Csonka, O. A. Vydrov, G. E. Scuseria, L. A. Constantin, X. Zhou, and K. Burke, *Phys. Rev. Lett.* **100**, 136406 (2008).
- [56] J. P. Perdew, K. Burke, and M. Ernzerhof, *Phys. Rev. Lett.* **77**, 3865 (1996).
- [57] See Supplemental Material [URL] for additional data and interpretations, which includes Refs. [65–68].
- [58] I. Errea, M. Calandra, and F. Mauri, *Phys. Rev. B* **89**, 064302 (2014).
- [59] R. Bianco, I. Errea, L. Paulatto, M. Calandra, and F. Mauri, *Phys. Rev. B* **96**, 014111 (2017).
- [60] L. Monacelli, R. Bianco, M. Cherubini, M. Calandra, I. Errea, and F. Mauri, *J. Phys.: Condens. Matter.* **33**, 363001 (2021).
- [61] W. Cochran, *Adv. Phys.* **9**, 387 (1960).
- [62] T. Ahsan, C.-H. Hsu, M. S. Hossain, and M. Z. Hasan,

- [Phys. Rev. Mater. \*\*7\*\*, 104204 \(2023\)](#).
- [63] C. Mielke, Y. Qin, J.-X. Yin, H. Nakamura, D. Das, K. Guo, R. Khasanov, J. Chang, Z. Q. Wang, S. Jia, S. Nakatsuji, A. Amato, H. Luetkens, G. Xu, M. Z. Hasan, and Z. Guguchia, [Phys. Rev. Mater. \*\*5\*\*, 034803 \(2021\)](#).
  - [64] I. Plokhikh, C. Mielke III, H. Nakamura, V. Petricek, Y. Qin, V. Sazgari, J. Küspert, I. Bialo, S. Shin, O. Ivashko, M. v. Zimmermann, M. Medarde, A. Amato, R. Khasanov, H. Luetkens, M. H. Fischer, M. Z. Hasan, J.-X. Yin, T. Neupert, J. Chang, G. Xu, S. Nakatsuji, E. Pomjakushina, D. J. Gawryluk, and Z. Guguchia, [arXiv \*\*10.48550/arXiv.2309.09255\*\* \(2023\)](#).
  - [65] G. Kresse and J. Furthmüller, [Comp. Mater. Sci. \*\*6\*\*, 15 \(1996\)](#).
  - [66] G. Kresse and J. Furthmüller, [Phys. Rev. B \*\*54\*\*, 11169 \(1996\)](#).
  - [67] P. E. Blöchl, [Phys. Rev. B \*\*50\*\*, 17953 \(1994\)](#).
  - [68] S. J. Clark, M. D. Segall, C. J. Pickard, P. J. Hasnip, M. I. J. Probert, K. Refson, and M. C. Payne, [Z. Kristallogr. \*\*220\*\*, 567 \(2005\)](#).

# Supplemental Material for “Origin of competing charge density waves in kagome metal $\text{ScV}_6\text{Sn}_6$ ”

Kang Wang,<sup>1</sup> Siyu Chen,<sup>1,2</sup> Sun-Woo Kim,<sup>1,\*</sup> and Bartomeu Monserrat<sup>1,2,†</sup>

<sup>1</sup>*Department of Materials Science and Metallurgy, University of Cambridge,  
27 Charles Babbage Road, Cambridge CB3 0FS, United Kingdom*

<sup>2</sup>*Cavendish Laboratory, University of Cambridge,  
J. J. Thomson Avenue, Cambridge CB3 0HE, United Kingdom*

## CONTENTS

1. Calculation details	2
2. Convergence tests	3
2.1. Convergence of phonon dispersions	3
2.2. Cross-check with CASTEP	5
3. Comparison between PBE and PBEsol functionals	6
3.1. Lattice parameters	6
3.2. Harmonic phonon dispersions	6
3.3. Potential energy surface along imaginary modes	7
4. Electronic temperature effects	8
5. CDW instabilities at zero temperature	9
6. Details about multi-phonon effects	10
7. Comparison with previous results	12
References	13



## 1. CALCULATION DETAILS

*Electronic structure calculations.* - We perform density functional theory (DFT) calculations using the Vienna *ab initio* simulation package VASP [1, 2] implementing the projector-augmented wave method [3]. We use PAW pseudopotentials with valence configurations:  $3s^23p^63d^14s^2$  ( $3d^14s^2$ ) for Sc atoms,  $3s^23p^64s^23d^3$  ( $4s^23d^3$ ) for V atoms, and  $5s^24d^{10}5p^2$  ( $5s^25p^2$ ) for Sn atoms for the cases with (without) semi-core states. We approximate the exchange correlation functional with the generalized-gradient approximation PBEsol [4] in the calculations reported in the main text. For comparison, we also perform calculations using the PBE [5] exchange-correlation functional. We use a kinetic energy cutoff for the plane wave basis of 500 eV and a Methfessel-Paxton smearing of 0.02 eV. We use a  $\Gamma$ -centered  $\mathbf{k}$ -point grid of size  $15 \times 15 \times 8$  for the primitive cell and commensurate  $\mathbf{k}$ -point grids for the supercell calculations. All the structures are optimized until the forces are below 0.005 eV/Å.

We perform a cross-check of the electronic structure calculations using the CASTEP [6] package, with norm-converging pseudopotentials generated on-the-fly (NCP19), and employing identical valence configurations as those used in VASP calculations, including semi-core states. We also use the PBEsol [4] exchange-correlation functional. We choose a kinetic energy cutoff for the plane wave basis of 1000 eV with a Gaussian smearing of 0.02 eV. We use a Monkhorst-Pack  $\mathbf{k}$ -point grid with an applied half step shift if the number of  $\mathbf{k}$ -points is even, which generates the exact same Gamma-centred  $\mathbf{k}$ -point grid as that used in the VASP calculations. All the structures are optimized until the forces are below 0.005 eV/Å.

*Harmonic phonon calculations.* - We perform harmonic phonon calculations using the finite displacement method in conjunction with nondiagonal supercells [7, 8]. The dynamical matrices are calculated on a Farey nonuniform  $\mathbf{q}$  grid [9] of size  $(3 \times 3 \times 2) \cup (3 \times 3 \times 3)$ , which is commensurate with both  $\mathbf{q}_2$  and  $\mathbf{q}_3$ . The final dynamical matrix is calculated through the force constant matrix on a target uniform  $\mathbf{q}$  grid of size  $3 \times 3 \times 6$ .

*Anharmonic phonon calculations.* - The anharmonic phonon calculations are performed using the stochastic self-consistent harmonic approximation (SSCHA) [10–12], which is a non-perturbation method taking into account anharmonic effects at both zero and finite temperature. The free energy of the real system is variationally minimized with respect to an auxiliary harmonic system. This is done using stochastic importance sampling, in which the total energy, forces, and stresses for an ensemble of configurations of the auxiliary harmonic system are calculated using VASP. The associated electronic structure calculations are performed using a kinetic energy cutoff 300 eV, and we consider configurations commensurate with a  $3 \times 3 \times 2$  supercell and a  $3 \times 3 \times 3$  supercell. The number of configurations needed to converge the free energy Hessian is of the order of 1,000. A Farey nonuniform  $\mathbf{q}$  grid of size  $(3 \times 3 \times 2) \cup (3 \times 3 \times 3)$  is used to get commensurate phonon results at both  $\mathbf{q}_2$  and  $\mathbf{q}_3$ . To get better prediction of the CDW transition temperature, the lattice parameters are fixed to the experimental values [13].

## 2. CONVERGENCE TESTS

### 2.1. Convergence of phonon dispersions

In this section, we investigate the convergence of phonon dispersions with respect to the  $\mathbf{q}$ -point grid size. Since the two competing CDW orders with wave vectors  $\mathbf{q}_2$  and  $\mathbf{q}_3$  correspond to the H and  $K'$  points of the Brillouin zone, respectively, it is crucial to calculate the dynamical matrices directly at both H and  $K'$  points to obtain reliable results. We accomplish this using a non-uniform Farey grid [14] of size  $(3 \times 3 \times 2) \cup (3 \times 3 \times 3)$ , as it is computationally more efficient than the uniform grid of size  $3 \times 3 \times 6$  that would otherwise be required.

Figure S1 shows the anharmonic phonon dispersions obtained with different  $\mathbf{q}$ -point grid sizes at various temperatures. The minimum uniform grid that includes both H and  $K'$  points would be of size  $3 \times 3 \times 6$ , which leads to a computationally prohibitive supercell size. Instead, we investigate the smaller  $\mathbf{q}$ -point grid of size  $3 \times 3 \times 2$  (blue solid lines), which includes the H point but does not include the  $K'$  point; and the smaller  $\mathbf{q}$ -point grid of size  $3 \times 3 \times 3$  (red solid lines), which includes the  $K'$  point but does not include the H point. The results in Fig. S1 demonstrate that the phonon frequencies at the H and  $K'$  points are significantly different depending on the  $\mathbf{q}$ -point grid used. At the harmonic level, the phonon frequencies at a given  $\mathbf{q}$ -point are exact if that point is included in the grid used. While this is not strictly true for anharmonic phonons, we still expect that the phonon frequencies at any given point will be more accurate when the grid includes that point, as relevant phonon-phonon interaction terms are directly included in the calculation. Therefore, we used a non-uniform Farey grid [14] of size  $(3 \times 3 \times 2) \cup (3 \times 3 \times 3)$ , which allows us to directly access both H and  $K'$  points without having to use prohibitively large supercells.

Using this strategy, the results in Fig. S1 show that when using a  $\mathbf{q}$ -point grid of size  $3 \times 3 \times 2$  (blue solid lines), the phonon frequencies at  $K'$ , which are obtained through Fourier interpolation, are higher than those obtained with the more accurate Farey grid (black dashed lines), leading to the absence of the  $\mathbf{q}_3$  CDW order even at  $T = 50$  K. Similarly, with the  $\mathbf{q}$ -point grid of size  $3 \times 3 \times 3$  (red solid lines), the phonon frequencies at H are interpolated, and are significantly lower than those obtained with the Farey grid (black dashed lines), resulting in them being imaginary even at  $T = 200$  K. These artificial features of Fourier interpolation can only be rectified by explicitly including both H and  $K'$  points, as done with the Farey grid (black dashed lines), and these are the results presented in the main text.

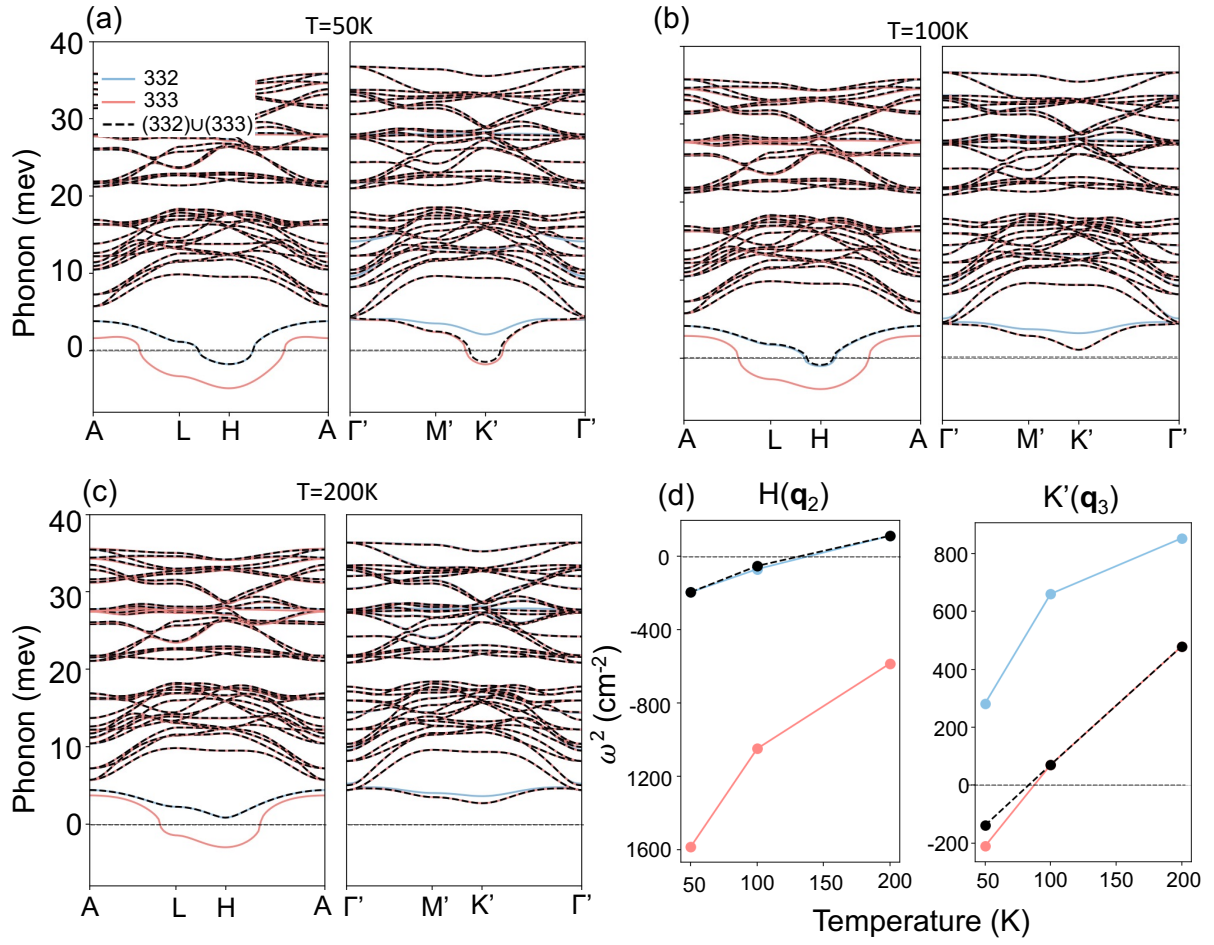


Figure S1. Calculated anharmonic phonon dispersions using  $\mathbf{q}$ -point grid sizes of  $3 \times 3 \times 2$ ,  $3 \times 3 \times 3$ , and  $(3 \times 3 \times 2) \cup (3 \times 3 \times 3)$  at (a) 50 K (b) 100 K and (c) 200 K. (d) The square of the lowest phonon frequency ( $\omega^2$ ) at the H ( $\mathbf{q}_2$ ) and  $K'$  ( $\mathbf{q}_3$ ) points.

## 2.2. Cross-check with CASTEP

To cross-check the results obtained from VASP, we perform calculations using CASTEP on the two CDW structures with the same valence configurations including semi-core states. The results from both VASP and CASTEP consistently show that the  $\mathbf{q}_3$  CDW order is stable over the  $\mathbf{q}_2$  CDW (Table S1). Specifically, the energy difference between the two CDW structures is 0.5 meV/f.u. and 1.1 meV/f.u. using VASP and CASTEP, respectively.

Table S1. The total energy (meV/f.u.) of fully relaxed CDW structures compared to pristine structure.

	$\mathbf{q}_2$ CDW	$\mathbf{q}_3$ CDW	$E(\mathbf{q}_2) - E(\mathbf{q}_3)$
VASP	-1.95	-2.42	0.47
CASTEP	-1.54	-2.66	1.12

### 3. COMPARISON BETWEEN PBE AND PBESOL FUNCTIONALS

#### 3.1. Lattice parameters

In the main text, we present the results obtained using the PBEsol exchange-correlation functional, as it yields a better agreement with the experimentally measured out-of-plane lattice parameter, a quantity that is crucial for CDW formation. Specifically, PBEsol gives an out-of-plane lattice parameter of  $c = 9.12 \text{ \AA}$ , which is closer to the experimental value of  $c = 9.16 \text{ \AA}$  compared to the PBE value of  $c = 9.25 \text{ \AA}$  (Table S2).

Table S2. Lattice parameters of pristine  $\text{ScV}_6\text{Sn}_6$  obtained using PBE and PBEsol.

Lattice parameter	PBE	PBEsol	Expt. [13]
In-plane $a$ ( $\text{\AA}$ )	5.46	5.39	5.47
Out-of-plane $c$ ( $\text{\AA}$ )	9.25	9.12	9.16

#### 3.2. Harmonic phonon dispersions

Figure S2 shows the calculated phonon dispersions using PBEsol and PBE. The overall phonon dispersions look similar, including the imaginary branches. Both PBEsol and PBE show phonon instabilities at the H and  $K'$  points, and the largest magnitude instability is observed at the H point.

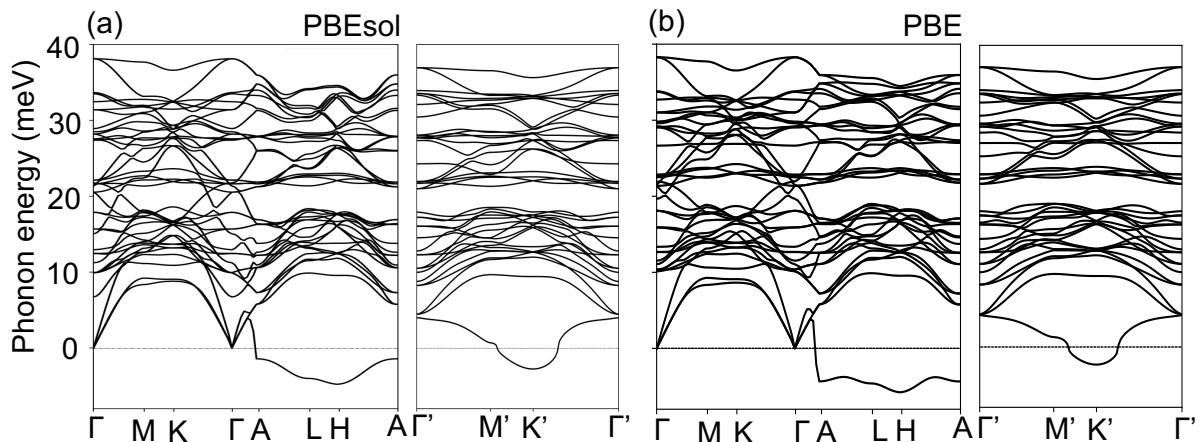


Figure S2. The harmonic phonon dispersions obtained using the (a) PBEsol and (b) PBE functionals. A Farey grid of size  $(3 \times 3 \times 2) \cup (3 \times 3 \times 3)$  is used to obtain the phonon dispersions.

### 3.3. Potential energy surface along imaginary modes

In Fig. 3 of the main text, we present the total energy of the  $\mathbf{q}_2$  and  $\mathbf{q}_3$  CDWs by displacing the pristine structure with a single phonon mode at H and  $K'$  points, respectively. Here, we provide the detailed calculation results and compare the results obtained using the PBE and PBEsol functionals. Figures S3(a) and S3(b) show the potential energy surface calculated using PBEsol with and without including the semi-core states in the valence. As discussed in the main text, the inclusion of the semi-core states reduces the energy gain of both CDW orders. Similarly, the PBE results [Figs. S3(c) and S3(d)] show a decrease in the energy gain of the CDW states upon including the semi-core states. It should be noted that the larger energy gain of the two CDW orders in PBE compared to PBEsol is due to the larger out-of-plane lattice parameter predicted by PBE, providing more space for distortion of Sn1-Sc-Sn1 trimers. Overall, both PBEsol and PBE consistently predict  $\mathbf{q}_2$  to be more stable distortion when a single phonon mode is considered.

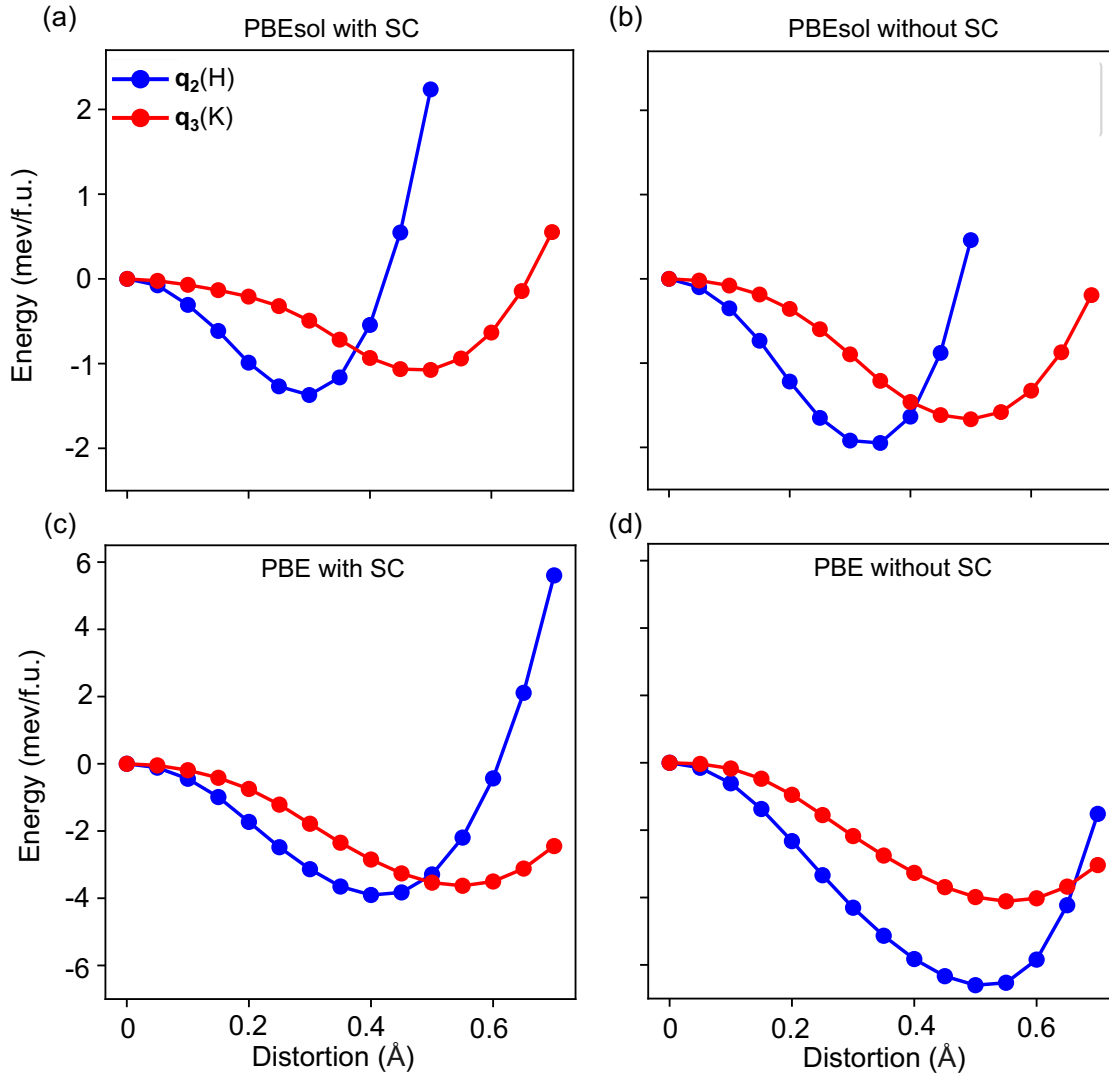


Figure S3. Calculated potential energy surface along the single phonon mode at the H ( $\mathbf{q}_2$ ) and  $K'$  ( $\mathbf{q}_3$ ) points. PBEsol results: (a) including and (b) excluding semi-core states in the valence. PBE results: (c) including and (d) excluding semi-core states in the valence.

#### 4. ELECTRONIC TEMPERATURE EFFECTS

In this section, we investigate the effects of electron temperature on harmonic phonon dispersions. We calculate harmonic phonon dispersions over a range of smearing values from 0.02 eV to 0.5 eV, corresponding approximately to temperatures ranging from 300 K to 5,800 K [Fig. S4(a)]. The phonon dispersions undergo changes with increasing electronic temperature, notably in the imaginary branches. Our results are similar to those of a previous study [15]. The estimated transition temperatures for the  $\mathbf{q}_2$  and  $\mathbf{q}_3$  CDWs are 5500 K and 2000 K, respectively [Fig. S4(b)].

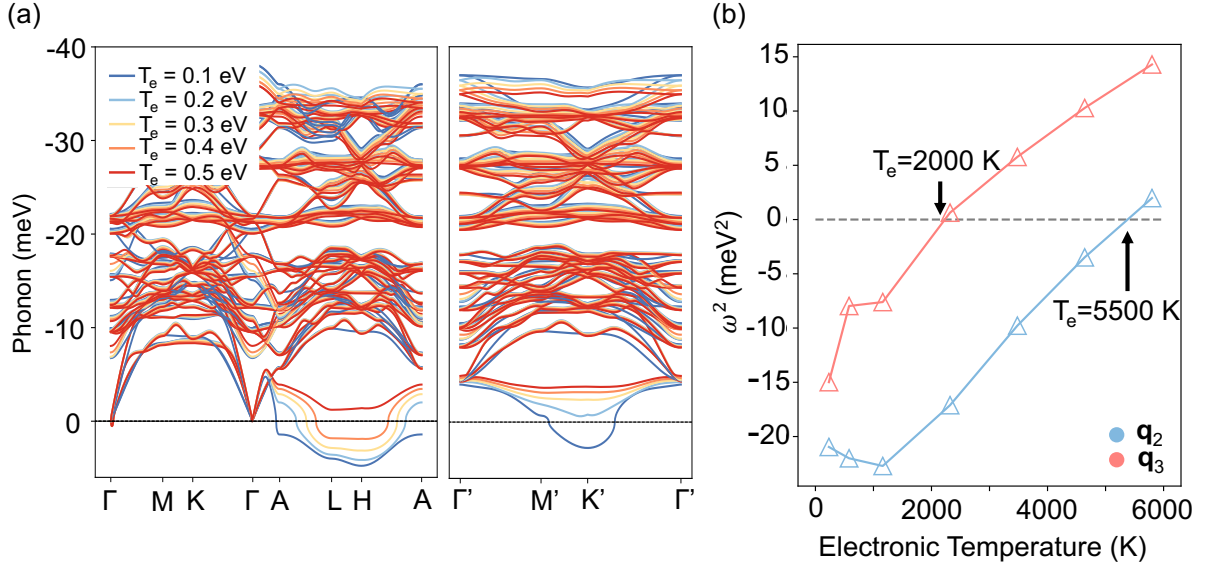


Figure S4. (a) The calculated harmonic phonon dispersion using various electronic temperature. (b) Squared phonon frequency  $\omega^2$  of the lowest energy phonon modes at the H and  $K'$  points with respect to the electronic temperature. Note that 0.1 eV is 1160.6 K.

## 5. CDW INSTABILITIES AT ZERO TEMPERATURE

As discussed in the main text, at finite temperatures, anharmonic phonon-phonon interactions lift most harmonic instabilities except those at the  $K'$  and  $H$  points, explaining experimental observations. At zero temperature, the anharmonic zero-point energy correction already lifts the harmonic instability at the  $A$  point, while CDW instabilities persist at the  $K'$ ,  $H$ , and  $L$  points [see Fig. 2(a) in the main text]. For completeness, this section delves into the energetics of these three CDW instabilities at zero temperature (Fig. S5), demonstrating that  $\mathbf{q}_3$  CDW is the most stable ground state, followed by the  $\mathbf{q}_2$  CDW. Our results show that the  $L$  CDW is the least stable at various levels of theory such that it cannot be observed even at very low temperatures.

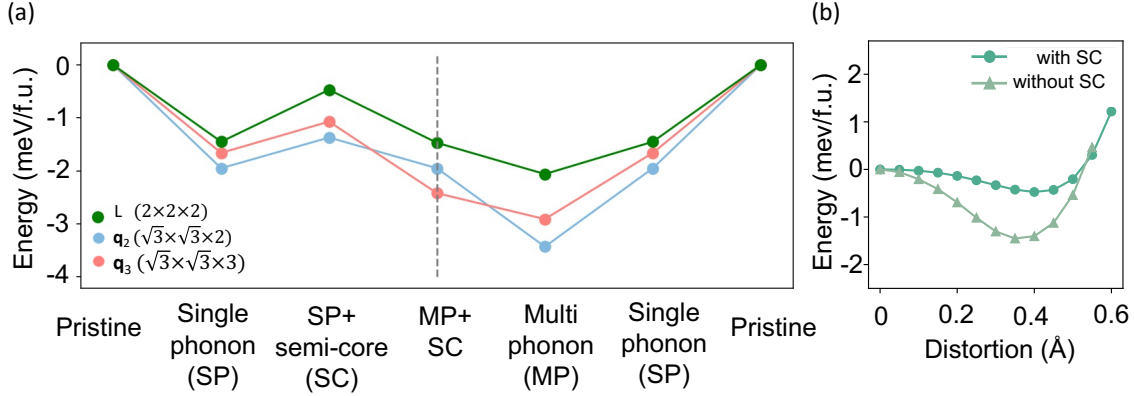


Figure S5. (a) Total energy of the  $\mathbf{q}_2, \mathbf{q}_3$  and  $L$  CDW structures compared to the pristine structure. Single phonon (SP) and multiple phonon (MP) indicate CDW structures distorted according to the atomic displacement pattern associated with a single phonon mode or with multiple phonon modes, respectively. Semi-core (SC) refer to calculations in which  $s$  and  $p$  semi-core states in  $Sc$  atoms and  $d$  semi-core states in  $Sn$  atoms are treated as valence states. (b) The potential energy surface of the  $L$  CDW structure.



## 6. DETAILS ABOUT MULTI-PHONON EFFECTS

In a typical potential energy surface calculation, the atoms of the high-symmetry pristine structure are distorted according to the displacement pattern provided by the eigenvector associated with the imaginary mode. For an imaginary mode, the resulting *single-mode* potential energy surface (Fig. S3) typically exhibits a “double-well” type shape, with the pristine structure corresponding to the central local maximum, surrounded by two minima that correspond to lower-energy structures. While the vast majority of potential energy surface calculations for CDW systems rely on this single-mode potential, there is no physical justification for this. The system will, in general, relax to the *overall* lowest energy point of the potential energy surface, and such a point may or may not correspond to the minima identified with the single-mode calculation. Therefore, *all* first principles calculations following an imaginary mode should be followed by a full relaxation, as we have done in our work. This subsequent relaxation will either leave the system unchanged (if the single-mode minimum is indeed the global minimum), or it will lead to a lower energy structure. Our calculations clearly reveal that in  $\text{ScV}_6\text{Sn}_6$ , these multi-phonon effects are critical to obtain the correct ground state (see Fig. 3 in the main text).

Having established the general principles behind relaxations starting from imaginary phonon modes, we move to discuss the case of  $\text{ScV}_6\text{Sn}_6$  in detail. In  $\text{ScV}_6\text{Sn}_6$ ,  $\mathbf{q}_3$  is associated with four degenerate modes:  $(\frac{1}{3}, \frac{1}{3}, \frac{1}{3})$ ,  $(-\frac{1}{3}, \frac{2}{3}, \frac{1}{3})$ ,  $(-\frac{1}{3}, -\frac{1}{3}, -\frac{1}{3})$  and  $(\frac{1}{3}, -\frac{2}{3}, -\frac{1}{3})$ . The corresponding eigenvectors are depicted in Fig. S6(a). Since they are degenerate, any linear combination of those four modes provides a valid basis for the degenerate subspace. By first distorting the structure along one of the four degenerate modes, and then relaxing it further, we allow for all harmonic degenerate modes to contribute irrespective of the arbitrary basis we started with. Using this procedure, in our calculations we confirm that first distorting the pristine structure along any of the four degenerate modes, and then further relaxing the structure ends up in the same CDW structure, which in all cases has a lower energy compared to the four single-mode structures. The structural difference between the final CDW structure and the initial high-symmetry pristine structure is shown in Fig. S6(b). Our final CDW structure is consistent with the experimentally reported CDW pattern.

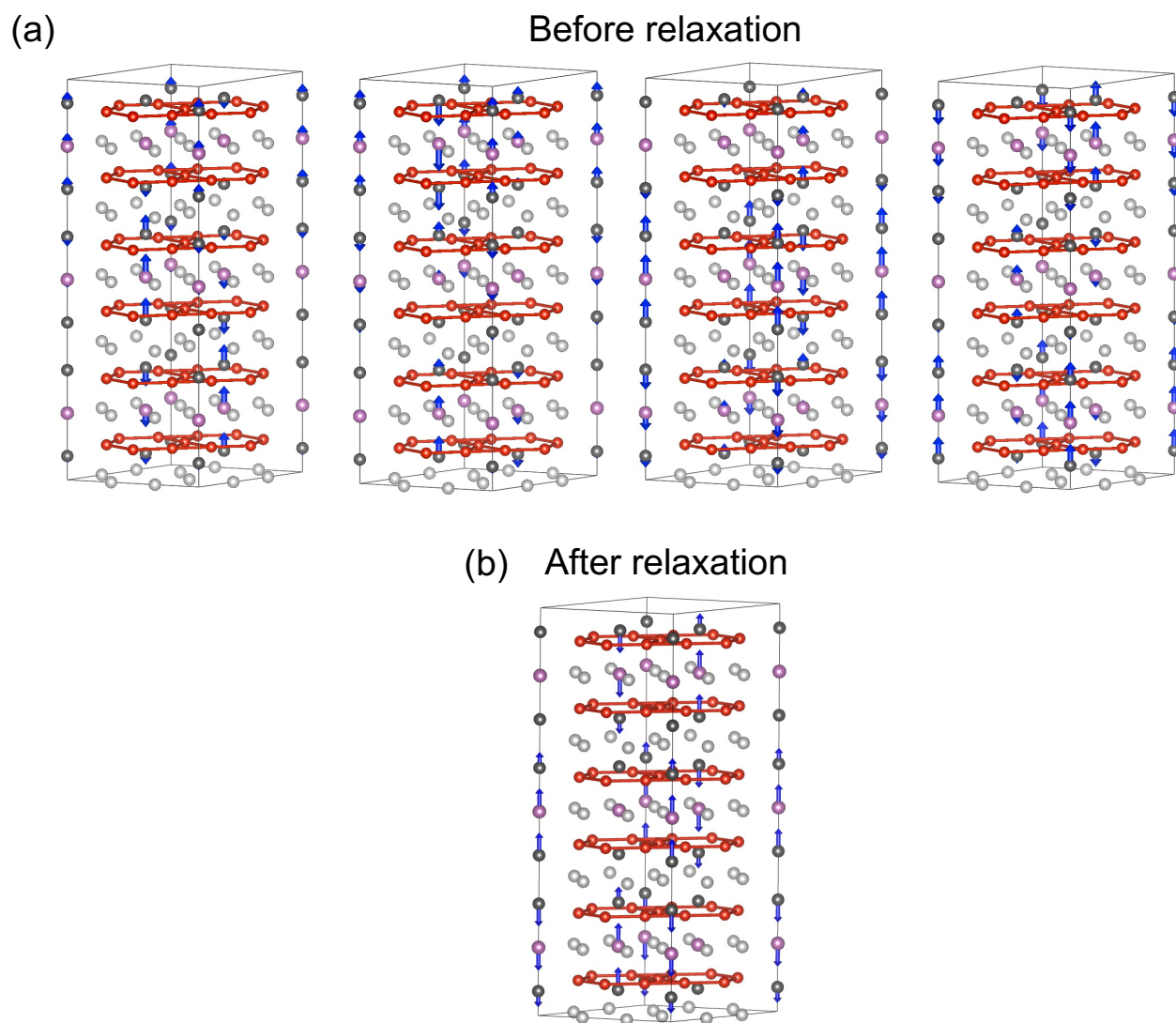


Figure S6. (a) The pristine structure with the arrows indicating the degenerate eigenmodes of  $\mathbf{q}_3$  (b) The pristine structure with the arrows indicating the structural difference between the pristine and the CDW structure after relaxation.

## 7. COMPARISON WITH PREVIOUS RESULTS

In this section, we calculate the energetics of the two competing CDW states as a function of the lattice parameter (Fig. S7). This allows us to rationalize the previous reports and explain why they obtained a  $\mathbf{q}_2$  CDW ground state rather than the experimentally observed  $\mathbf{q}_3$  CDW ground state. The previous DFT calculations [15–19] were performed using the PBE functional, yielding an optimized out-of-plane lattice parameter of  $c = 9.25 \text{ \AA}$ , which is significantly larger than the experimental out-of-plane lattice parameter of  $c = 9.16 \text{ \AA}$  [13]. At the PBE-optimized lattice parameters, the  $\mathbf{q}_2$  CDW is indeed calculated to be more stable than the  $\mathbf{q}_3$  CDW (triangle in Fig. S7). However, using the experimentally reported lattice parameters shows the  $\mathbf{q}_3$  CDW is ground state (star in Fig. S7). These results confirm the important role that the out-of-plane lattice parameter plays in determining the relative stability of the two CDW orders. The results also explain why previous DFT calculations failed to predict the  $\mathbf{q}_3$  CDW ground state even if some of them considered the inclusion of the semi-core states in the valence states.

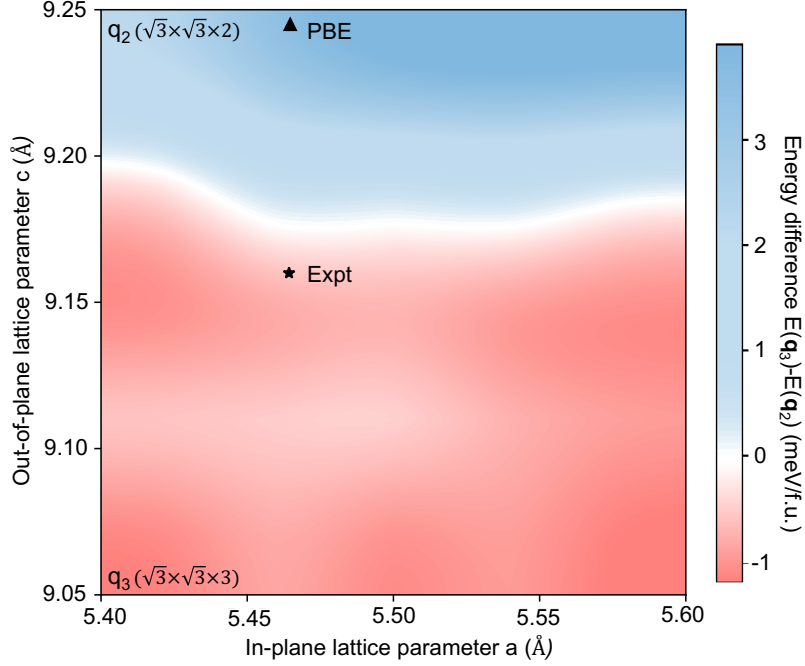


Figure S7. Calculated phase diagram as a function of lattice parameters using the PBE functional. The color bar represents the energy difference between the  $\mathbf{q}_2$  and  $\mathbf{q}_3$  CDW structures. The triangle corresponds to the lattice parameters obtained using the PBE functional, while the star represents the lattice parameters reported experimentally [13].

---

\* [swk38@cam.ac.uk](mailto:swk38@cam.ac.uk)

† [bm418@cam.ac.uk](mailto:bm418@cam.ac.uk)

- [1] G. Kresse and J. Furthmüller, *Comp. Mater. Sci.* **6**, 15 (1996).
- [2] G. Kresse and J. Furthmüller, *Phys. Rev. B* **54**, 11169 (1996).
- [3] P. E. Blöchl, *Phys. Rev. B* **50**, 17953 (1994).
- [4] J. P. Perdew, A. Ruzsinszky, G. I. Csonka, O. A. Vydrov, G. E. Scuseria, L. A. Constantin, X. Zhou, and K. Burke, *Phys. Rev. Lett.* **100**, 136406 (2008).
- [5] J. P. Perdew, K. Burke, and M. Ernzerhof, *Phys. Rev. Lett.* **77**, 3865 (1996).
- [6] S. J. Clark, M. D. Segall, C. J. Pickard, P. J. Hasnip, M. I. J. Probert, K. Refson, and M. C. Payne, *Z. Kristallogr.* **220**, 567 (2005).
- [7] J. H. Lloyd-Williams and B. Monserrat, *Phys. Rev. B* **92**, 184301 (2015).
- [8] B. Monserrat, *J. Phys. Condens. Matter* **30**, 083001 (2018).
- [9] S. Chen, P. T. Salzbrenner, and B. Monserrat, *Phys. Rev. B* **106**, 155102 (2022).
- [10] I. Errea, M. Calandra, and F. Mauri, *Phys. Rev. B* **89**, 064302 (2014).
- [11] R. Bianco, I. Errea, L. Paulatto, M. Calandra, and F. Mauri, *Phys. Rev. B* **96**, 014111 (2017).
- [12] L. Monacelli, R. Bianco, M. Cherubini, M. Calandra, I. Errea, and F. Mauri, *J. Phys.: Condens. Matter.* **33**, 363001 (2021).
- [13] H. W. S. Arachchige, W. R. Meier, M. Marshall, T. Matsuoka, R. Xue, M. A. McGuire, R. P. Hermann, H. Cao, and D. Mandrus, *Phys. Rev. Lett.* **129**, 216402 (2022).
- [14] S. Chen, P. T. Salzbrenner, and B. Monserrat, *Phys. Rev. B* **106**, 155102 (2022).
- [15] H. Hu, Y. Jiang, D. Călugăru, X. Feng, D. Subires, M. G. Vergniory, C. Felser, S. Blanco-Canosa, and B. A. Bernevig, *arXiv* [10.48550/arXiv.2305.15469](https://arxiv.org/abs/10.48550/arXiv.2305.15469) (2023).
- [16] H. Tan and B. Yan, *Phys. Rev. Lett.* **130**, 266402 (2023).
- [17] S. Liu, C. Wang, S. Yao, Y. Jia, Z. Zhang, and J.-H. Cho, *arXiv* [10.48550/arXiv.2308.13796](https://arxiv.org/abs/10.48550/arXiv.2308.13796) (2023).
- [18] A. Subedi, *arXiv* [10.48550/arXiv.2308.11553](https://arxiv.org/abs/10.48550/arXiv.2308.11553) (2023).
- [19] S. Cao, C. Xu, H. Fukui, T. Manjo, Y. Dong, M. Shi, Y. Liu, C. Cao, and Y. Song, *Nat. Commun.* **14**, 7671 (2023).